Designing catalyst layer morphology for high-performance water electrolysis using synchrotron X-ray nanotomography

Lee, Jason Keonhag; Kim, Pascal; Krause, Kevin; Shrestha, Pranay; Balakrishnan, Manojkumar; Fahy, Kieran; Fatih, Khalid; Shaigan, Nima; Ge, Mingyuan; Lee, Wah-Keat; Bazylak, Aimy

Publisher's version / Version de l'éditeur:
https://doi.org/10.1016/j.xcrp.2022.101232
Cell Reports Physical Science, 4, 1, 2023-01-10

Cell Reports
Physical Science

CellPress
OPEN ACCESS

Article

Designing catalyst layer morphology for high-performance water electrolysis using synchrotron X-ray nanotomography

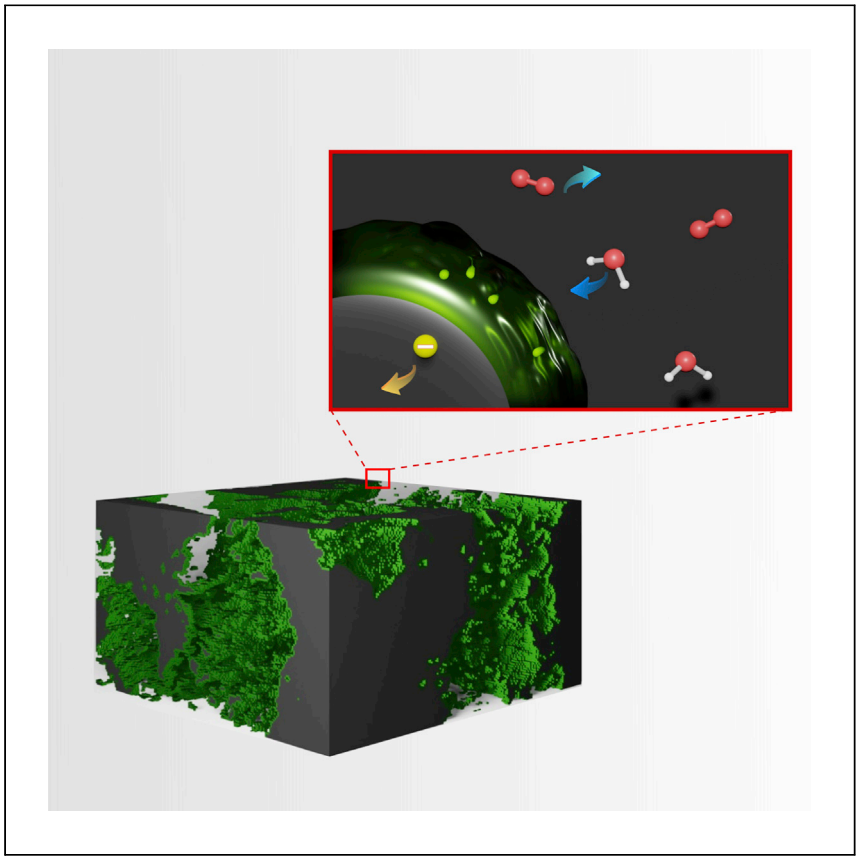

Water electrolyzers are needed for decarbonization, but catalyst loadings must be reduced due to iridium shortages. Here, Lee et al. demonstrate the combined use of synchrotron transmission X-ray microscopy and pore network modeling to predict conductivities and transport behavior for designing next-generation ultra-low loading catalyst layers.

Jason Keonhag Lee, Pascal Kim, Kevin Krause, ..., Mingyuan Ge, Wah-Keat Lee, Aimy Bazylak

aimy.bazylak@utoronto.ca

Highlights

Ultra-high-resolution 3D computed tomography imaging of iridium-based catalyst layer

Pore network modeling on nanostructured PEM water electrolyzer catalyst layer

Modeling conductivities and mass transport properties of catalyst layers

Lee et al., Cell Reports Physical Science 4, 101232
January 18, 2023
https://doi.org/10.1016/j.xcrp.2022.101232

Cell Reports
Physical Science

CellPress
OPEN ACCESS

Article

Designing catalyst layer morphology for high-performance water electrolysis using synchrotron X-ray nanotomography

Jason Keonhag Lee,[1] Pascal Kim,[1] Kevin Krause,[1] Pranay Shrestha,[1] Manojkumar Balakrishnan,[1] Kieran Fahy,[1] Khalid Fatih,[2] Nima Shaigan,[2] Mingyuan Ge,[3] Wah-Keat Lee,[3] and Aimy Bazylak[1,4,*]

SUMMARY

The limited availability of iridium in the Earth's crust poses severe challenges to establishing gigawatt-scale electrolyzers that are needed for energy storage; this problem urgently calls for reduced iridium loadings. Reducing iridium loadings requires catalyst structure optimization, but to date, little attention has been paid to the characterization of electron, proton, and mass transport in the catalyst layer, particularly at the nanoscale. We present the 3D nanoscale pore structure of iridium-based catalyst layers via synchrotron full-field transmission X-ray microscopy (TXM) and perform pore network modeling to determine effective transport properties in water electrolyzers. We observe a wide range of pore sizes in the catalyst layer, constituting pathways that facilitate mass transport. Increasing the thickness of the ionomer layer that covers the catalyst particles significantly increases protonic conductivity at the cost of reducing the open pore space and electrical conductivity, both of which are detrimental to electrolyzer performance.

INTRODUCTION

The widespread production and use of hydrogen are critically needed to reduce the production of greenhouse gas emissions and facilitate the electrification of energy and transportation sectors. As an energy carrier, hydrogen serves as the currency needed to balance energy demand and supply through flexible storage, thereby enabling the electrification of transportation, stationary, and portable power generation sectors through fuel cell technologies.[1] Despite the promise of hydrogen, today, the majority of hydrogen is generated by reforming hydrocarbons (gray hydrogen), which is responsible for emitting approximately 830 million tons of carbon dioxide per year.[2] There is a pressing need for hydrogen production powered by renewable energy (green hydrogen) to complete the decarbonization of the energy sector and in turn provide the energy security that is now constantly under threat due to extreme weather events that accompany climate change.

Polymer electrolyte membrane (PEM) water electrolysis is particularly attractive for its ability to function in dynamic (part-load and overload) conditions, making it ideal for integration with intermittent renewables to produce high-purity green hydrogen.[3] Various megawatt-scale PEM electrolyzer plants are being installed around the world, such as the 10 MW PEM water electrolyzer plant installed in 2018 as a part of the European Union (EU) project REFHYNE.[4] To meet the growing demand for green hydrogen, PEM water electrolyzer plants must be scaled up even further to the gigawatt (GW) range.[5]

[1]Thermofluids for Energy and Advanced Material Laboratory, Department of Mechanical and Industrial Engineering, Faculty of Applied Science and Engineering, University of Toronto, Toronto, ON M5S 3G8, Canada

[2]National Research Council Canada, 4250 Wesbrook Mall, Vancouver, BC V6T 1W5, Canada

[3]National Synchrotron Light Source II, Brookhaven National Laboratory, Building 743 Ring Road, Upton, NY 11973, USA

[4]Lead contact

*Correspondence: aimy.bazylak@utoronto.ca

https://doi.org/10.1016/j.xcrp.2022.101232

The corrosive environment of the oxygen evolution reaction combined with the highly oxidizing conditions in the anode (>2 V) pose major constraints to the material selection of the anode compartment. At the current scale of PEM electrolyzer production, the catalysts constitute ~8% of the stack cost.[6,7] While ~8% may seem relatively low compared with the other associated costs of electrolyzers, the cost of the catalyst layer is prohibitive when scaling up to the GW range that is critically needed. Shirvanian and van Berkel predict that for every GW of capacity, approximately 500 kg of iridium will be required for PEM electrolysis.[7] Iridium in the amount of 500 kg is staggering considering the scarcity of iridium; the production rate of iridium is less than 9,000 kg per year.[8] Hence, there is an urgent need to develop ultra-low loading catalyst layers for high-performance PEM water electrolyzers.

Recent literature has shown that novel catalyst designs and fabrication techniques can be used to enhance the performance of water splitting at reduced loadings.[9–12] Similar to how carbon supports are used for Pt catalysts in PEM fuel cells, support materials have also been developed for PEM electrolyzers to reduce the iridium loadings required while enhancing electrical conductivity.[9] Carbon supports cannot be used for water splitting due to the harsh environment of the oxygen evolution reaction. TiO_2 supports are promising, but there is room for significant improvement in terms of reaching ideal electrical conductivities.[10] Regmi et al. addressed the issue of low electrical conductivity by adding a layer of Pt between the TiO_2 and iridium.[11] A recent study demonstrated that mass transport losses play a critical role when ultra-low iridium catalysts loadings are used (~0.011 mg/cm^2).[12] Electrolyzer performance was most susceptible to mass transport losses at these ultra-low loadings; therefore, an improved understanding of mass transport behavior is vitally needed for designing next-generation catalyst layers. Examining mass transport mechanisms in the porous transport layer of an electrolyzer already poses significant challenges due to the range of relevant length scales and material opacity,[13–15] and even more complex mechanisms are at play in the catalyst layer; the conduction of electrons in the iridium, the conduction of ions in the ionomer layer, the delivery of reactant liquid water to the reaction sites, and the removal of product gas from the reaction sites must all be considered in the design of the catalyst structure.

The microstructure of the catalyst layer is what governs the performance of the electrolyzer.[16] Ionomers bind the catalyst particles together, and the characteristics of the resulting microstructure depend on factors such as the rheology of the ink (catalyst and ionomer dispersed in water/alcohol mixture) and coating methods.[17] Alia et al.[18] demonstrated that varying ink and spray parameters both have significant impacts on the catalyst structure, thereby influencing electrolyzer performance and durability. Khandavalli et al.[17] showed that the ratio of the ionomer and catalyst in the ink and its resultant agglomeration size are important parameters that affect the agglomeration of the catalyst particles. Typically, catalyst inks are characterized via techniques such as dynamic light scattering[17] and X-ray scattering.[19,20] Cetinbas et al. have developed hybrid methods using multiple characterization techniques to analyze fuel cell catalyst layers.[21] While these techniques provide valuable information about the catalyst microstructure, such as agglomeration distribution, oxidation state, and dissolution measurement, these traditional methods are not sufficient to correlate structural properties to transport properties. Modeling presents a new paradigm in understanding the catalyst structure of electrochemical devices. Specifically, pore-scale models have been previously implemented to estimate multiphase reactive transport in the cathode catalyst layer of a PEM fuel cell.[22] While these comprehensive pore-scale models disclose interactions between multi-phase flow and reactive transport in fuel cell catalysts, the impact of 3D morphology of the

catalyst layer on multi-phase transport remains ambiguous because of high computational load. A new approach is needed to determine the impact of the microstructure on critical properties, such as protonic conductivity, electrical conductivity, and permeability in 3D morphology, to design optimized catalysts for high-performance and low-loading catalyst layers.

In this work, we determine the relationship between structural properties and transport properties in catalyst layers of a PEM electrolyzer using a characterization technique based on 3D nanoscale imaging and pore network modeling. The 3D structure of the commercially available iridium-based catalyst is examined via synchrotron full-field transmission X-ray microscopy (TXM) at nanoscale resolution. Then, pore network modeling is used to explore the impact of catalyst microstructure on electrical and protonic conductivities as well as single- and two-phase permeability for liquid water and gas. Pore network modeling exhibits both the computational efficiency and the pore-scale resolution needed to simulate mass transport directly in the computational domains obtained through our TXM scans. This newly proposed characterization technique can be used to design catalyst microstructures for next-generation PEM water electrolyzers and other electrochemical energy-conversion technologies.

RESULTS AND DISCUSSION

Characterizing catalyst layer structure via transmission X-ray tomography

The high pixel resolution of 30 nm/pixel and spatial resolution of <50 nm/pixel obtained from the synchrotron full-field TXM reveals the 3D pore structure of the iridium-based catalyst used in electrolyzers. The reconstruction of the iridium-based catalyst sample is shown in Figure 1A (5.55 × 5.55 × 3 μm), illustrating the existence of pores ranging from tens of nanometers to a few microns in the catalyst layer. This wide range of pore sizes in the iridium-based catalyst structure is particularly evident in the cross-sectional image (a slice of the reconstruction image, Figure 1B). Both pores at the tens of nanometers and at a few microns in diameter contribute to catalyst utilization as long as the triple boundary phase (the catalyst, ionomer, and reactant liquid water) exists at the site. However, we speculate that mass transport of the reactant liquid water and product oxygen gas mainly occurs in the macro pores of the catalyst layer since macro pores play a key role in permeability. Although pores with diameters below our imaging resolution exist in the sample, the permeability of these pores would be orders of magnitude lower than the macro pores.

The pore size distribution of the iridium-based catalyst structure is seen in Figure 1C. While the majority of pores exhibit diameters less than 200 nm (with mean pore diameter of the structure being 203 nm), a large number of macro pores are visible in the catalyst structure. Assuming capillary-dominated flow takes place over this range of pore sizes, the largest pores exhibiting the lowest capillary pressures provide dominant pathways for gas removal, while the smaller pores exhibiting the highest capillary pressures provide key pathways for liquid water transport. The agglomerate size distribution of iridium-based catalyst particles (iridium agglomerates) is shown in Figure 1D. Since the size of the individual iridium particle is below our imaging resolution, we present the iridium phase in the form of agglomerates, which we obtained by extracting the solid network from the TXM images. The sizes of the agglomerates inform the degree to which iridium is dispersed within the catalyst layer, which impacts the electrical and protonic conductivities. The iridium agglomerates are larger than the surrounding pores, with most agglomerates less

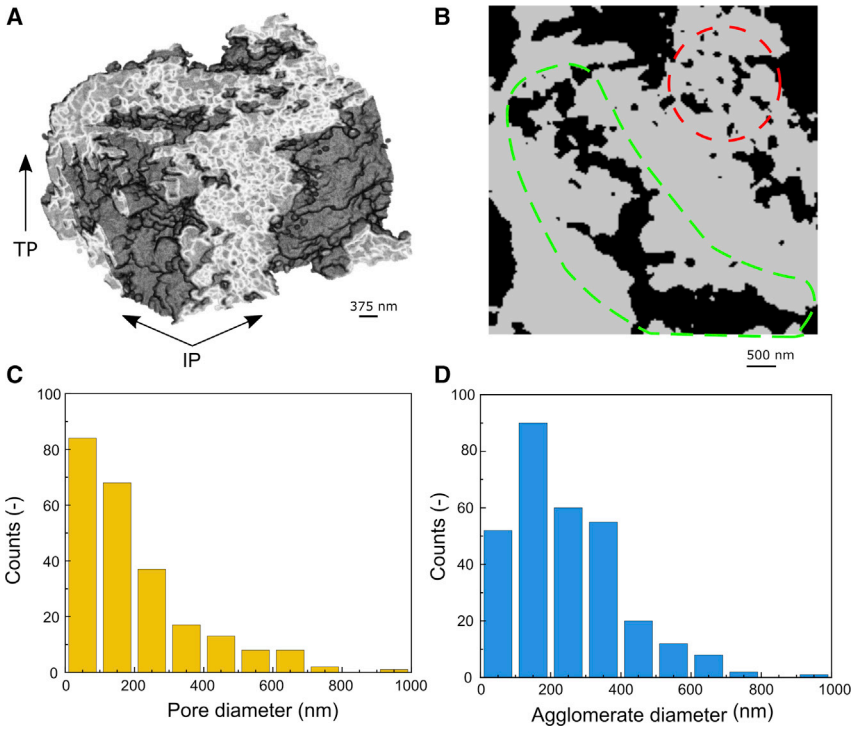

Figure 1. Structural characterization of iridium-based catalyst

(A) 3D reconstruction of the iridium-based catalyst obtained via synchrotron full-field transmission X-ray microscopy (TXM) acquired from the Full-Field X-ray Imaging (FXI) beamline (18-ID) of National Synchrotron Light Source II (NSLS-II). Colors are used for visualization purposes only. The scale bar represents 375 nm.

(B) A cross-sectional image of the iridium-based catalyst revealing the wide range of pore sizes. The scale bar represents 500 nm.

(C and D) A pore size distribution (C) and an agglomerate size distribution (D) of the iridium-based catalyst.

than 400 nm in diameter (mean agglomerate diameter: ~247 nm). The pore size and agglomerate size distributions for other iridium-based samples show similar trends, as seen in Figures 1C and 1D (Figures S3 and S4). The agglomerate size distribution is crucial for electrolyzer catalysts because the common catalyst materials used for electrolyzers suffer from low electrical conductivity. For fuel cell catalysts, Pt supported on carbon is used for enhanced conductivity, but this does not extend to electrolyzers due to the highly corrosive environment. Therefore, finding the appropriate agglomerate size distribution that provides high electrical conductivity is key to increasing catalyst utilization. TXM coupled with pore network modeling is powerful for quantifying structural properties of catalyst layers from electrolyzer stacks.

Electrical conductivity and mass transport in catalyst layer structure

The schematic describing the process of transport calculations is shown in Figure S9. The effective electrical conductivity and permeability (one phase and two phase) are calculated for in-plane (IP) and through-plane (TP) directions to characterize the iridium-based catalyst layer (Figure 2A). The IP and TP directions are parallel and perpendicular to the membrane/catalyst layer interface, respectively. In both directions, the effective electrical conductivity is approximately 8 S/cm, which is comparable to the values reported in the literature.[23–25] The effective electrical conductivity determined from samples 2 and 3 also show similar values (Figures S5 and S6). However, values of the single-phase permeability vary significantly with direction.

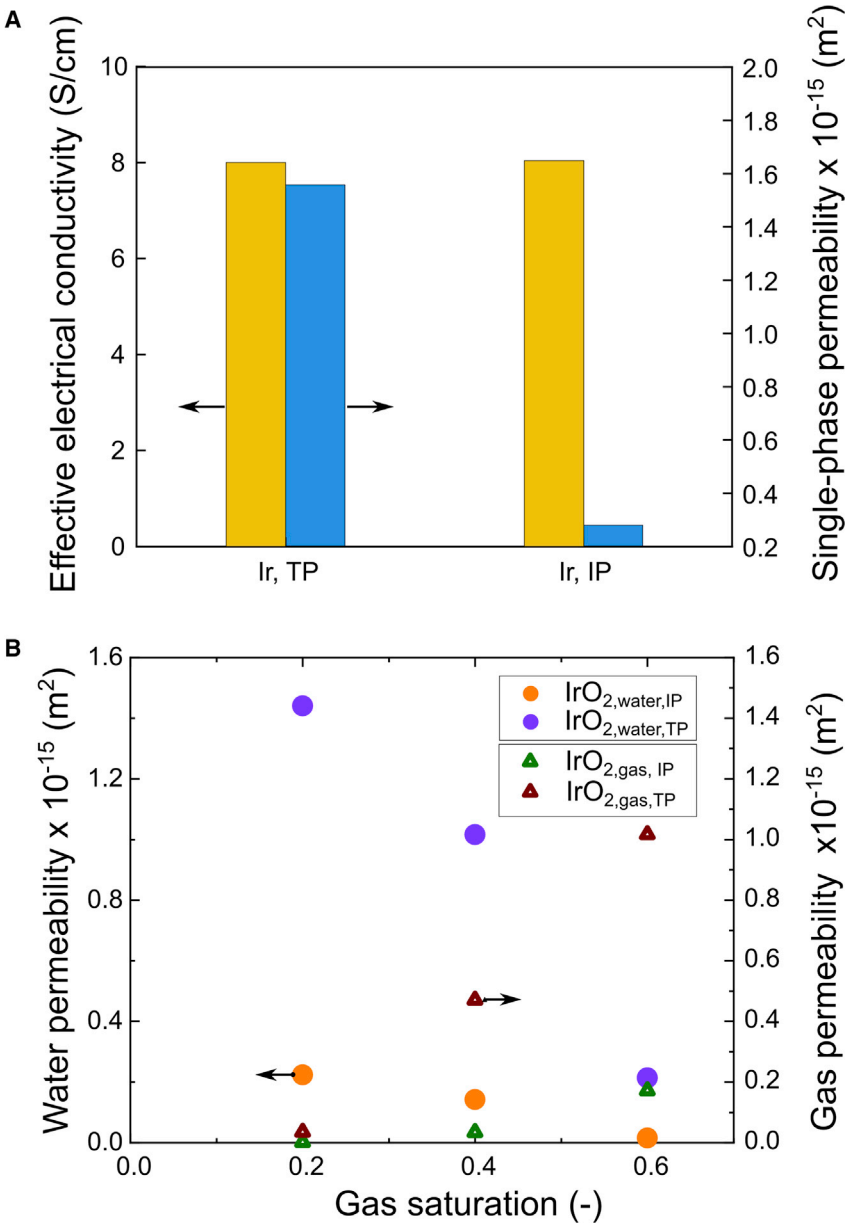

Figure 2. Comparing the electrical conductivity and mass transport properties in the in-plane and through-plane directions

(A) Effective electrical conductivity and single-phase permeability of the iridium-based catalyst in both the through-plane (TP) direction and in-plane (IP) direction. Transport in the catalyst structure takes place preferentially in the TP direction.

(B) Two-phase permeability of liquid water and gas as a function of gas saturation. The circle markers refer to the left y axis (water permeability), and triangle markers refer to the right y axis (gas permeability).

Specifically, the single-phase permeability is an order of magnitude higher for the TP direction compared with the IP direction (Figure 2A). This result reveals that mass transport pathways in the TP direction toward the porous transport layer dominate in comparison to the lateral transport pathways across the pores of the catalyst layer; therefore, designing the interface between the catalyst layer and porous transport layer is key for effective mass transport behavior.

To elucidate the transport properties of the iridium-based catalyst structure, we calculate the two-phase permeability of liquid water and gas. In this model, a pore is considered impermeable to one phase when it is occupied by the other phase, i.e., if a pore is occupied by gas, then liquid water cannot permeate through that pore when calculating the two-phase permeability. Since mass transport mechanisms within the catalyst layer are still elusive within the field,[12,26] we stochastically select pores to be filled with gas based on a uniform distribution (of the total number of pores) until target saturations are obtained (20%, 40%, and 60% gas saturation). While in our previous work for porous transport layers (PTLs),[15,27–29] we used drainage (non-wetting phase invading wetting phase driven by capillary forces) to simulate gas invasion and obtain gas saturation, here we apply stochastic pore invasion since the precise nature of multi-phase flow in the catalyst layer has yet to be experimentally validated.

The two-phase permeability of liquid water is an indicator of effective reactant delivery to the reaction sites, and the two-phase permeability of gas is an indicator of effective gas removal from the reaction sites. Both liquid water and gas exhibit preferential transport in the TP direction (Figure 2B), thereby indicating the importance of the interface between the catalyst layer and the PTL. Furthermore, we observe that gas saturation determines which transport pathways dominate within the catalyst layer: liquid transport pathways or gas transport pathways. Specifically, at a gas saturation of 20%, the liquid water permeability is orders of magnitude higher than the gas permeability, while the opposite is observed for a gas saturation of 60%. While it is generally accepted that product gas accumulation in the anode PTL leads to mass transport limitations,[14,26,30–35] here, for the first time, we demonstrate the role that gas saturation in the catalyst layer plays in tuning the liquid and gas phase permeabilities of the catalyst layer, which ultimately governs the electrochemical performance of the PEM water electrolyzer.

Controlling the ionomer layer

To investigate the impact of controlling the ionomer layer, we numerically added an ionomer layer onto the nano-computed tomography (CT) image at varying thicknesses: 30, 60, and 90 nm (Figure 3). With the addition of the ionomer layer onto the catalyst structure, we observe that pores in a range of tens of nanometers in the catalyst become completely filled with the ionomer phase, i.e., these closed pores will inhibit mass transport pathways (Figure 3). Furthermore, the effective electrical conductivity of the catalyst structure decreases with the addition of the ionomer layer since ionomer phases are electrically insulated. To compensate for this reduction in effective electrical conductivity, we removed iridium in an amount equivalent to the thickness of the ionomer added, and we recalculated the effective electrical conductivity. Here, we show for the first time the significant impact of ionomer content on electrical conductivity, namely that the effective electrical conductivity reduces by 2 S/cm with the addition of a 30 nm ionomer layer (Figure 4A).

We also provide new insight into how ionomer layer thickness contributes to effective protonic conductivity of the 3D catalyst structure. Along with reactant and electron conduction, ionic conductivity is also important for initiating the oxygen evolution reaction. Therefore, the catalyst structure in the electrolyzer must ensure sufficient protonic conductivity. When an ionomer layer of uniform thickness (30 nm) is added to the 3D catalyst structure, the catalyst exhibits an effective protonic conductivity of only 0.003 mS/cm, which indicates that catalyst particles far from the membrane are less likely to participate in the oxygen evolution reaction

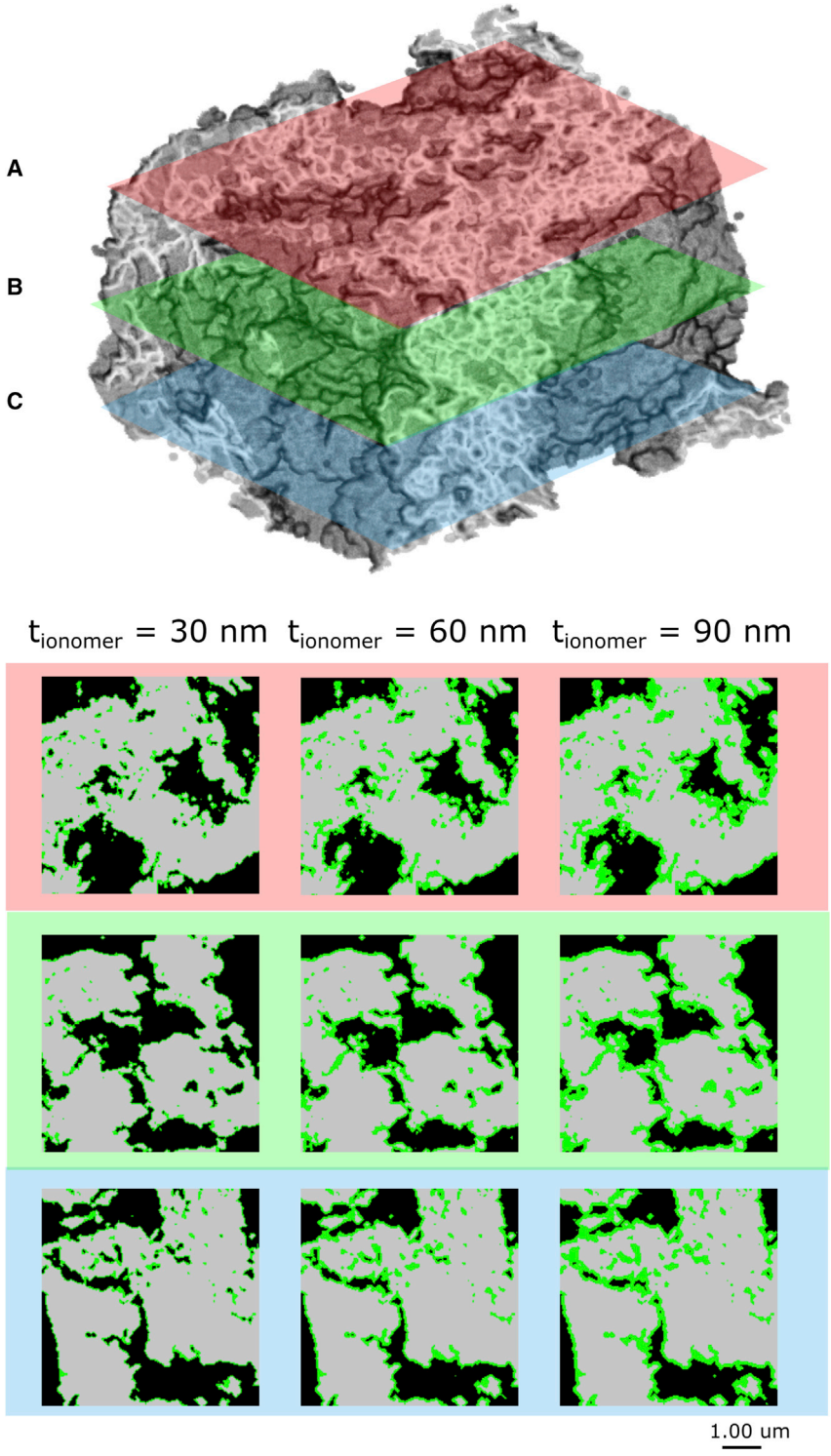

Figure 3. Ir catalyst structure with added layers of the ionomer

Cross-sectional images at (A) 5%, (B) 50%, and (C) 95% of the thickness of the iridium-based catalyst. Ionomer layers have been added with thicknesses of 30, 60, and 90 nm. Some pores with diameters at tens of nanometers in the catalyst become closed as the thickness of the ionomer layer is increased. The scale bar represents 1.00 μm.

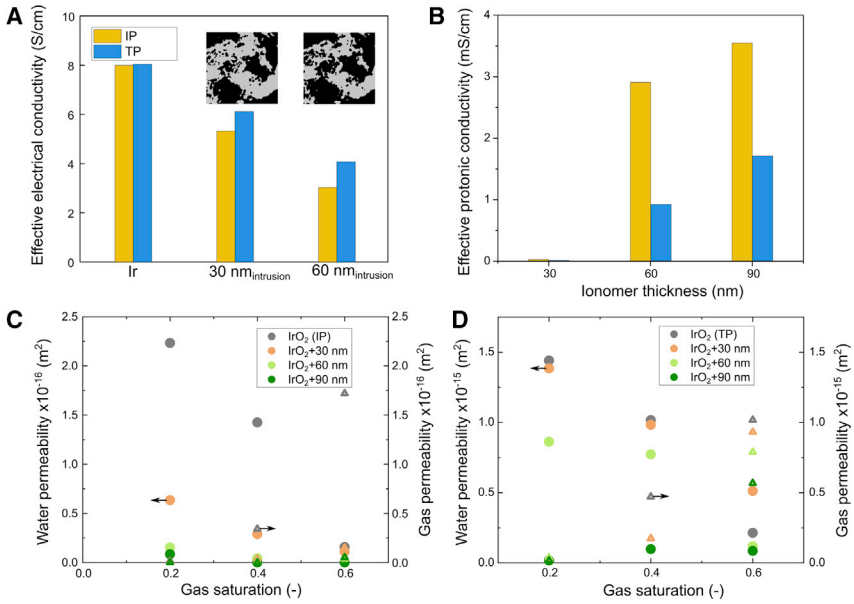

Figure 4. Characterization of iridium-based catalyst with varying ionomer layer thicknesses

(A) Change in effective electrical conductivity in the presence of an ionomer layer.

(B) Effective protonic conductivity with varying ionomer layer thicknesses.

(C and D) Two-phase permeability of gas and liquid water at varying levels of gas saturation in the (C) IP direction and the (D) TP direction. The circle markers refer to the left y axis (water permeability), and triangle markers refer to the right y axis (gas permeability).

due to the low ionic conductivity. However, depositing a 60-nm-thick ionomer layer significantly increases the protonic conductivity to 2.9 mS/cm, and this trend continues as thicker ionomer layers are added (Figure 4B). In addition, we observe that effective protonic conductivity is more favorable in the IP direction compared with the TP direction.

The ionomer displaces otherwise void pore volume in the catalyst layer; therefore, the transport properties of the catalyst layer are strongly affected by changes in the ionomer volume. The number of smaller pores in the catalyst structure decreases with the addition of ionomer (Figure S2). The porosity of the catalyst structure without the addition of the ionomer layer is 39%, but the porosity decreases to 20.7% with the addition of a 90-nm-thick ionomer layer (Table 1). As expected, the permeability of both liquid water and gas are greatly reduced when the ionomer content of the catalyst structure increases (Figures 4C and 4D). We observe that the mean pore diameter is not affected by the ionomer thickness, and we attribute this to the tendency for the ionomer to mainly fill the smallest pores (i.e., the number of pores decreases). In fact, the addition of the ionomer closes smaller transport pathways in the catalyst layer, and as a result, the permeability values decrease especially in the IP direction. With the thickest ionomer layer, we speculate that severe mass transport issues will occur in the catalyst layer as the permeability values of both water and gas in the IP direction are lower than 1×10^{-17} m^2. Low values of permeabilities arising from having thicker ionomer layers are also seen from samples 2 and 3 (Figures S7 and S8). The multi-phase transport mechanism of protons, electrons, reactants, and products are summarized in Figure 5. We believe that fine-tuning the ionomer layer thickness is crucial for fabricating catalyst layers that exhibit high electrical and protonic conductivities and effective mass transport properties.

Table 1. Structural and transport properties of the commercially available iridium-based catalyst structure with varying ionomer thicknesses

Ionomer thickness (nm)	Ionomer volume (%)	Porosity (–)	Mean pore diameter (m)	Single-phase permeability (IP) (m^2)	Single-phase permeability (TP) (m^2)
0	0	0.387	2.03×10^{-7}	2.79×10^{-16}	1.56×10^{-15}
30	7.86	0.308	1.99×10^{-7}	7.02×10^{-17}	1.48×10^{-15}
60	13.6	0.251	2.02×10^{-7}	2.68×10^{-17}	1.04×10^{-15}
90	18	0.207	2.19×10^{-7}	9.20×10^{-18}	8.31×10^{-16}

In this work, we are the first to illustrate the impact of controlling the ionomer layer within a PEM catalyst layer on mass, electronic, and protonic transport. We comprehensively characterize the catalyst layer structure of a commercial iridium-based catalyst-coated membrane for water electrolysis using synchrotron full-field TXM and pore network modeling. TXM results reveal that the catalyst structure consists of nano and macro pores and iridium agglomerates that provide mass transport and electron conduction pathways. The pore network modeling results show higher effective protonic conductivity in the IP direction and higher permeabilities in the TP direction. Moreover, we reveal that increasing the thickness of the ionomer layer in the catalyst layer significantly reduces both the effective electrical conductivity and two-phase permeability because the ionomer occupies pore volumes in the catalyst structure. This newly proposed combination of TXM and pore network modeling for PEM water electrolyzers is promising for characterizing and tuning catalyst structures with effective protonic conductivity, effective electrical conductivity, and transport properties as a function of gas saturation.

EXPERIMENTAL PROCEDURES

Resource availability

Lead contact

Further information and requests for resources should be directed to and will be fulfilled by the lead contact, Aimy Bazylak (aimy.bazylak@utoronto.ca).

Materials availability

This study did not generate new unique reagents.

Data and code availability

The data supporting the findings of this study are available within the article and supplemental information. Other related data are available from the lead contact upon request.

Full-field TXM

The 3D structure of a commercially available iridium-based catalyst layer was captured using TXM at the Full-Field X-ray Imaging (FXI) beamline (18-ID) at the National Synchrotron Light Source II (NSLS-II). The high-flux photons from the synchrotron source enabled a pixel (px) resolution of 30 nm/px with a sub-50 nm/px spatial resolution. A temporal resolution of approximately 6 min per scan was obtained with the setup. The specific details of the FXI beamline can be found in the following literature.[36] In this work, 6 kV synchrotron radiation was used to scan iridium catalyst samples at an exposure time of 0.2 s/frame, and 1,600 projections were taken. The rotation speed was set to 0.5 deg/s, and filters were not applied to the beam.

The catalyst layer sample was obtained from a commercially available iridium-based catalyst coated membrane (HYDrion, Ion Power) with an iridium loading of 1.0 mg/cm^2 on a Nafion N115 membrane. Catalyst particles were thinly grazed

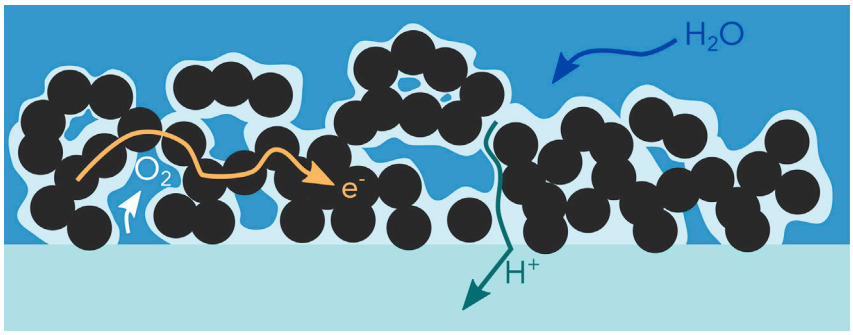

Figure 5. Schematic summarizing the multi-phase transport mechanism occurring at the catalyst layer

Protons transport within the ionomer phase in both IP and TP directions. Oxygen gas and liquid water transport in both IP and TP directions through the pores existing in the catalyst layer. Electrons are transferred through the iridium particles.

away from the membrane using a sharp blade under the optical microscope, and the catalyst particles were positioned and adhered to a flat-head pin substrate using a small amount of epoxy. Images were obtained from the central region of the sample to avoid any potentially intruded epoxy in the catalyst layer. Once the catalyst sample was prepared, the pin was mounted on a sample holder available at the FXI beamline. The schematic of the TXM was as shown in Figure S1.

Image processing and pore network extraction

The collected tomographic images of the catalyst structure were first reconstructed using the "Gridrec" available in TomoPy. Flat-field and dark-field images were used to normalize the intensity in the images, and no further image alignment was performed other than finding the center of the rotation during the reconstruction process. For the segmentation process of the reconstructed images, Otsu's method for thresholding was implemented to distinguish between the iridium and void phase. Through this method, the threshold values can be determined by computing the minimum of the sum of weighted variances of the grayscale values. This method was applied to every TP grayscale slice in the reconstruction to obtain an array of threshold values. The value of the mode from this threshold array was applied to the entire stack to ensure consistent binary segmentation. Median filtering (radius = 1) was applied to improve the signal-to-noise ratio. The images were cropped from the central region of the catalyst sample to avoid edge effects and to mitigate epoxy infiltration, which resulted in the domain size of the domain being $5.55 \times 5.55 \times 3\ \mu m$.

The pore network of an iridium-based catalyst was next obtained through the process of pore network extraction. A customized watershed algorithm available in the open-source Python package PoreSpy[37] was used to perform pore network extraction. A maximum filter (radius = 4) and a Gaussian filter (sigma = 0.4) were used in this work. The connectivity of the iridium phase was obtained via the extraction process. Isolated pores and isolated solid particles were removed from the pore network and did not contribute to transport simulations as they do not contribute to permeability and conduction.

Addition of ionomer layers

In this experiment, the ionomer was not distinguished from other phases due to the nature of synchrotron X-ray beams. Therefore, the ionomer layer was numerically

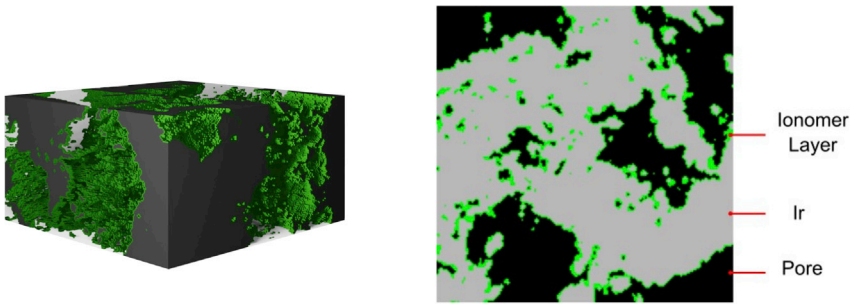

Figure 6. Cross section of the iridium-based catalyst with the addition of an ionomer layer
The gray region is the iridium phase, the black region is the pore/void phase, and the green layer is the ionomer with a thickness of 1 pixel (30 nm).

added by first identifying the interface between the iridium phase and the void in the TXM images (Figure 6). Since the resolution of the image was 30 nm/px, the minimum thickness of the added ionomer phase was limited to a minimum of 30 nm. The ionomer layer, which provides proton conduction pathways in the catalyst layer, was numerically added as shown in Figure 1 as the green layer. For the 30-nm-thick ionomer phase, the ionomer layer was 1-px-thick, and for the 90 nm ionomer phase, the layer was 3-px-thick. For simplicity, we assumed a uniform ionomer thickness. We acknowledge that in realistic conditions, ionomers do not necessarily uniformly coat the catalyst particles. However, a uniform layer of ionomer will provide valuable insight to the significant impact on both transport and material properties of the catalyst structure.

Permeability calculation

Permeability is a key transport property in the PTL of a PEM water electrolyzer, where pore sizes range from a micron to tens of microns. However, despite the importance of effective transport within the electrolyzer catalyst layer, the details of these transport mechanisms still elude the field due to the scarcity of advanced imaging and numerical simulations at relevant length scales. In this work, we use permeability as an indicator of transport properties in the iridium-based catalyst structure. We compute two distinct permeability values: single-phase permeability and two-phase permeability of gas and liquid water. The single-phase permeability is a property of the porous structure (i.e., catalyst layer) describing the effectiveness of single-phase flow in the porous media (when only one phase exists). Two-phase permeability is the effectiveness of one phase flow in the presence of other phases in the porous media. In the application of electrolysis, the two-phase permeability refers to liquid water in the presence of oxygen gas or gas in the presence of liquid water. In our model, the pores occupied by the second phase (i.e., gas when calculating water permeability or water when calculating gas permeability) are considered closed (impermeable) pores. The two-phase permeability of liquid water represents the reactant delivery to the reaction sites, and two-phase permeability of gas represents the effective gas removal from the reaction sites. More details regarding our pore network modeling approach can be found from our previous studies.[15,27]

First, the flow rate and pressure drop in the pore network are determined by solving the mass conservation equation at each pore:

$$q_i = \sum_{j=1}^{n} g_{h,ij}\left(P_j - P_i\right) = 0, \qquad \text{(Equation 1)}$$

where i and j represent the current and neighboring pores, respectively; q_i indicates the net flow in pore i ($m^3 \cdot s^{-1}$); $g_{h,ij}$ is the hydraulic conductivity of flow of each neighboring pore ($m^4 \cdot s \cdot kg^{-1}$); and P is the pressure in each pore ($kg \cdot m^{-1} \cdot s^{-2}$). The Hagen-Poiseuille model for a flow through a cylindrical duct is used to obtain the hydraulic conductivity:[38]

$$g_h = \frac{\pi r^4}{8L\mu}, \quad \text{(Equation 2)}$$

where L and r are the length and the radius of the pore or throat (m), respectively, and μ refers to the dynamic viscosity ($kg \cdot m^{-1} \cdot s^{-1}$). Linear resistor theory with values of hydraulic conductivities for one-half of a pore i, the connecting throat, and one-half of a pore j are used to calculate the net hydraulic conductivity:

$$\frac{1}{g_{h,ij}} = \frac{1}{g_{h,pi}} + \frac{1}{g_{h,t}} + \frac{1}{g_{h,pj}} \quad \text{(Equation 3)}$$

Solving Equation 1 as a set of linear equations with the prescribed pressure boundary conditions at the outlets of the network gives the total flow, Q ($m^3 \cdot s^{-1}$), across the network. With Q determined, we solve Darcy's law to calculate permeability of the catalyst structure:

$$Q = \frac{KA}{\mu l}(P_{in} - P_{out}), \quad \text{(Equation 4)}$$

where K is permeability (m^2), A is the cross-sectional area (m^2), P_{in} and P_{out} are applied inlet and outlet boundary pressures, respectively, and l is the length along the direction of flow (m).

Effective conductivity calculation

Pore network modeling was used to calculate effective electrical conductivity and effective protonic conductivity of the iridium-based catalyst layer. To calculate effective electrical conductivity of the catalyst layer, the iridium phase from the TXM images was represented as a network of spheres connected by cylindrical conduits using the pore network extraction process, as described above. The resultant network provided the connectivity of the iridium phase of the TXM images. The electrical conductivity of the catalyst layer in both the IP and TP directions was then obtained by calculating the sphere-to-sphere electrical conductance from the extracted solid network. A bulk electrical conductance value of 25.9 S/cm[39] for irregular iridium nanoparticles was used for our simulations. To account for losses in electrical conductivity due to the presence of ionomer layers, an amount of iridium phase equal to the thickness of the ionomer layer was removed. To investigate the impact of ionomer layer thickness on mass transport, the permeability was calculated for the iridium catalyst structure with reduced pore sizes and porosity due to the addition of controlled ionomer layers. The effective protonic conductivity of the catalyst layer for both the IP and TP directions was computed similarly to electrical conductance but using a solid network extracted from the ionomer phase instead of the iridium phase, and an ionic resistance of 95 mS/cm[40] was applied.

SUPPLEMENTAL INFORMATION

Supplemental information can be found online at https://doi.org/10.1016/j.xcrp.2022.101232.

ACKNOWLEDGMENTS

This work was supported by the Natural Sciences and Engineering Research Council of Canada (NSERC) Discovery Grants Program and the Canada Research Chairs

Program. Graduate scholarships awarded to J.K.L. from NSERC Alexander Graham Bell Canada Graduate Scholarships – Doctoral Program, Queen Elizabeth II/Edward Rygiel Graduate Scholarship in Science and Technology, Ontario Graduate Scholarship, and Glynn Williams Fellowships are also gratefully acknowledged. This research used the 18-ID beamline of the NSLS-II, a US Department of Energy (DOE) Office of Science User Facility operated for the DOE Office of Science by Brookhaven National Laboratory under contract no. DE-SC0012704.

AUTHOR CONTRIBUTIONS

Conceptualization, J.K.L.; data curation, J.K.L. and A.B.; formal analysis, J.K.L. and A.B.; funding acquisition, A.B.; investigation, J.K.L., P.K., K.K., P.S., M.B., K. Fahy, K. Fatih, N.S., M.G., W.-K.L., and A.B.; methodology, J.K.L., P.K., K.K., P.S., M.B., K. Fahy, M.G., W.-K.L., and A.B.; validation, J.K.L., M.G., and W.-K.L.; visualization, J.K.L.; writing – original draft, J.K.L. and A.B.; writing – review & editing, J.K.L., P.K., K.K., P.S., M.B., K. Fahy, K. Fatih, N.S., M.G., W.-K.L., and A.B.; resources, M.G., W.-K.L., and A.B.; software, M.G. and W.-K.L.; project administration, A.B.; supervision, A.B.

DECLARATION OF INTERESTS

A.B. is a member of the *Cell Reports Physical Science* advisory board.

Received: February 19, 2022
Revised: September 29, 2022
Accepted: December 15, 2022
Published: January 10, 2023

REFERENCES

1. Barbir, F., and Yazici, S. (2008). Status and development of PEM fuel cell technology. Int. J. Energy Res. *32*, 369–378. https://doi.org/10.1002/er.1371.

2. IEA (2019). The Future of Hydrogen – Analysis (IEA). https://www.iea.org/reports/the-future-of-hydrogen.

3. Carmo, M., Fritz, D.L., Mergel, J., and Stolten, D. (2013). A comprehensive review on PEM water electrolysis. Int. J. Hydrog. Energy. *38*, 4901–4934. https://doi.org/10.1016/j.ijhydene.2013.01.151.

4. REFHYNE. Clean Refinery Hydrogen for Europe. https://refhyne.eu/.

5. Bernt, M., Hartig-Weiß, A., Tovini, M.F., El-Sayed, H.A., Schramm, C., Schröter, J., Gebauer, C., and Gasteiger, H.A. (2020). Current challenges in catalyst development for PEM water electrolyzers. Chemie Ing. Tech. *92*, 31–39. https://doi.org/10.1002/cite.201900101.

6. Bertuccioli, L., Chan, A., Hart, D., Lehner, F., Madden, B., and Standen, E. (2014). Development of Water Electrolysis in the European Union. https://www.fch.europa.eu/node/783.

7. Shirvanian, P., and van Berkel, F. (2020). Novel components in proton exchange membrane water electrolyzers (PEMWE): status, challenges and future needs. Electrochem. commun. *114*, 106704. https://doi.org/10.1016/j.elecom.2020.106704.

8. Vesborg, P.C.K., and Jaramillo, T.F. (2012). Addressing the terawatt challenge: scalability in the supply of chemical elements for renewable energy. RSC Adv. *2*, 7933–7947. https://doi.org/10.1039/c2ra20839c.

9. Karimi, F., and Peppley, B.A. (2017). Metal carbide and oxide supports for iridium-based oxygen evolution reaction electrocatalysts for polymer-electrolyte-membrane water electrolysis. Electrochim. Acta *246*, 654–670. https://doi.org/10.1016/j.electacta.2017.06.048.

10. Mazúr, P., Polonský, J., Paidar, M., and Bouzek, K. (2012). Non-conductive TiO 2 as the anode catalyst support for PEM water electrolysis. Int. J. Hydrog. Energy *37*, 12081–12088. https://doi.org/10.1016/j.ijhydene.2012.05.129.

11. Regmi, Y.N., Tzanetopoulos, E., Zeng, G., Peng, X., Kushner, D.I., Kistler, T.A., King, L.A., and Danilovic, N. (2020). Supported oxygen evolution catalysts by design: toward lower precious metal loading and improved conductivity in proton exchange membrane water electrolyzers. ACS Catal. *10*, 13125–13135. https://doi.org/10.1021/acscatal.0c03098.

12. Taie, Z., Peng, X., Kulkarni, D., Zenyuk, I.V., Weber, A.Z., Hagen, C., and Danilovic, N. (2020). Pathway to complete energy sector decarbonization with available iridium resources using ultralow loaded water electrolyzers. ACS Appl. Mater. Interfaces *12*, 52701–52712. https://doi.org/10.1021/acsami.0c15687.

13. Angulo, A., van der Linde, P., Gardeniers, H., Modestino, M., and Fernández Rivas, D. (2020). Influence of bubbles on the energy conversion efficiency of electrochemical reactors. Joule *4*, 555–579. https://doi.org/10.1016/j.joule.2020.01.005.

14. Lee, J.K., and Bazylak, A. (2021). Bubbles: the good, the bad, and the ugly. Joule *5*, 19–21. https://doi.org/10.1016/J.JOULE.2020.12.024.

15. Lee, J.K., Lee, C.H., and Bazylak, A. (2019). Pore network modelling to enhance liquid water transport through porous transport layers for polymer electrolyte membrane electrolyzers. Power Sources *437*, 226910. https://doi.org/10.1016/j.jpowsour.2019.226910.

16. Holdcroft, S. (2013). Fuel cell catalyst layers: a polymer science perspective. Chem. Mater. *26*, 381–393. https://doi.org/10.1021/CM401445H.

17. Khandavalli, S., Park, J.H., Kariuki, N.N., Zaccarine, S.F., Pylypenko, S., Myers, D.J., Ulsh, M., and Mauger, S.A. (2019). Investigation of the microstructure and rheology of iridium oxide catalyst inks for low-temperature polymer electrolyte membrane water electrolyzers. ACS Appl. Mater. Interfaces *11*, 45068–45079. https://doi.org/10.1021/acsami.9b14415.

18. Alia, S.M., Reeves, K.S., Baxter, J.S., and Cullen, D.A. (2020). The impact of ink and spray variables on catalyst layer properties, electrolyzer performance, and electrolyzer durability. J. Electrochem. Soc. *167*, 144512. https://doi.org/10.1149/1945-7111/ABC746.

19. Abbott, D.F., Lebedev, D., Waltar, K., Povia, M., Nachtegaal, M., Fabbri, E., Copéret, C., and Schmidt, T.J. (2016). Iridium oxide for the oxygen evolution reaction: correlation between particle size, morphology, and the surface hydroxo layer from operando XAS. Chem. Mater. *28*, 6591–6604. https://doi.org/10.1021/ACS.CHEMMATER.6B02625.

20. Povia, M., Abbott, D.F., Herranz, J., Heinritz, A., Lebedev, D., Kim, B.-J., Fabbri, E., Patru, A., Kohlbrecher, J., Schäublin, R., et al. (2019). Operando X-ray characterization of high surface area iridium oxides to decouple their activity losses for the oxygen evolution reaction. Energy Environ. Sci. *12*, 3038–3052. https://doi.org/10.1039/C9EE01018A.

21. Cetinbas, F.C., Ahluwalia, R.K., Kariuki, N., De Andrade, V., Fongalland, D., Smith, L., Sharman, J., Ferreira, P., Rasouli, S., and Myers, D.J. (2017). Hybrid approach combining multiple characterization techniques and simulations for microstructural analysis of proton exchange membrane fuel cell electrodes. Power Sources *344*, 62–73. https://doi.org/10.1016/J.JPOWSOUR.2017.01.104.

22. Paliwal, S., Panda, D., Bhaskaran, S., Vorhauer-Huget, N., Tsotsas, E., and Surasani, V.K. (2021). Lattice Boltzmann method to study the water-oxygen distributions in porous transport layer (PTL) of polymer electrolyte membrane (PEM) electrolyser. Int. J. Hydrog. Energy *46*, 22747–22762. https://doi.org/10.1016/J.IJHYDENE.2021.04.112.

23. Schuler, T., Ciccone, J.M., Krentscher, B., Marone, F., Peter, C., Schmidt, T.J., and Büchi, F.N. (2020). Hierarchically structured porous transport layers for polymer electrolyte water electrolysis. Adv. Energy Mater. *10*, 1903216. https://doi.org/10.1002/aenm.201903216.

24. Kosakian, A., and Secanell, M. (2020). Estimating charge-transport properties of fuel-cell and electrolyzer catalyst layers via electrochemical impedance spectroscopy. Electrochim. Acta *367*, 137521. https://doi.org/10.1016/j.electacta.2020.137521.

25. Puthiyapura, V.K., Mamlouk, M., Pasupathi, S., Pollet, B.G., and Scott, K. (2014). Physical and electrochemical evaluation of ATO supported IrO2 catalyst for proton exchange membrane water electrolyser. J. Power Sources *269*, 451–460. https://doi.org/10.1016/j.jpowsour.2014.06.078.

26. Lee, C., Lee, J.K., Zhao, B., Fahy, K.F., and Bazylak, A. (2020). Transient gas distribution in porous transport layers of polymer electrolyte membrane electrolyzers. J. Electrochem. Soc. *167*, 024508. https://doi.org/10.1149/1945-7111/ab68c8.

27. Lee, J.K., and Bazylak, A. (2020). Optimizing porous transport layer design parameters via stochastic pore network modelling: reactant transport and Interfacial contact considerations. J. Electrochem. Soc. *167*, 013541. https://doi.org/10.1149/1945-7111/ab6557.

28. Stiber, S., Balzer, H., Wierhake, A., Wirkert, F.J., Roth, J., Rost, U., Brodmann, M., Lee, J.K., Bazylak, A., Waiblinger, W., et al. (2021). Porous transport layers for proton exchange membrane electrolysis under extreme conditions of current density, temperature, and pressure. Adv. Energy Mater. *11*, 2100630. https://doi.org/10.1002/AENM.202100630.

29. Stiber, S., Sata, N., Morawietz, T., Ansar, S.A., Jahnke, T., Lee, J.K., Bazylak, A., Fallisch, A., Gago, A.S., and Friedrich, K.A. (2022). A high-performance, durable and low-cost proton exchange membrane electrolyser with stainless steel components. Energy Environ. Sci. *15*, 109–122. https://doi.org/10.1039/D1EE02112E.

30. Lopata, J., Kang, Z., Young, J., Bender, G., Weidner, J.W., and Shimpalee, S. (2020). Effects of the transport/catalyst layer interface and catalyst loading on mass and charge transport phenomena in polymer electrolyte membrane water electrolysis devices. J. Electrochem. Soc. *167*, 064507. https://doi.org/10.1149/1945-7111/ab7f87.

31. Lee, J.K., Lee, C., Fahy, K.F., Zhao, B., LaManna, J.M., Baltic, E., Jacobson, D.L., Hussey, D.S., and Bazylak, A. (2020). Critical current density as a performance indicator for gas-evolving electrochemical devices. Cell Rep. Phys. Sci. *1*, 100147. https://doi.org/10.1016/j.xcrp.2020.100147.

32. Lee, J.K., Lee, C., Fahy, K.F., Kim, P.J., Krause, K., LaManna, J.M., Baltic, E., Jacobson, D.L., Hussey, D.S., and Bazylak, A. (2020). Accelerating bubble detachment in porous transport layers with patterned through-pores. ACS Appl. Energy Mater. *3*, 9676–9684. https://doi.org/10.1021/acsaem.0c01239.

33. De Angelis, S., Schuler, T., Charalambous, M.A., Marone, F., Schmidt, T.J., and Büchi, F.N. (2021). Unraveling two-phase transport in porous transport layer materials for polymer electrolyte water electrolysis. J. Mater. Chem. *9*, 22102–22113. https://doi.org/10.1039/D1TA03379D.

34. Maier, M., Dodwell, J., Ziesche, R., Tan, C., Heenan, T., Majasan, J., Kardjilov, N., Markötter, H., Manke, I., Castanheira, L., et al. (2020). Mass transport in polymer electrolyte membrane water electrolyser liquid-gas diffusion layers: a combined neutron imaging and X-ray computed tomography study. J. Power Sources *455*, 227968. https://doi.org/10.1016/j.jpowsour.2020.227968.

35. Leonard, E., Shum, A.D., Normile, S., Sabarirajan, D.C., Yared, D.G., Xiao, X., and Zenyuk, I.V. (2018). Operando X-ray tomography and sub-second radiography for characterizing transport in polymer electrolyte membrane electrolyzer. Electrochim. Acta *276*, 424–433. https://doi.org/10.1016/j.electacta.2018.04.144.

36. Ge, M., Coburn, D.S., Nazaretski, E., Xu, W., Gofron, K., Xu, H., Yin, Z., and Lee, W.K. (2018). One-minute nano-tomography using hard X-ray full-field transmission microscope. Appl. Phys. Lett. *113*, 083109. https://doi.org/10.1063/1.5048378.

37. Gostick, J.T. (2017). Versatile and efficient pore network extraction method using marker-based watershed segmentation. Phys. Rev. E *96*, 023307. https://doi.org/10.1103/PhysRevE.96.023307.

38. Bryant, S., and Blunt, M. (1992). Prediction of relative permeability in simple porous media. Phys. Rev. A *46*, 2004–2011. https://doi.org/10.1103/PhysRevA.46.2004.

39. Lim, J., Park, D., Jeon, S.S., Roh, C.-W., Choi, J., Yoon, D., Park, M., Jung, H., and Lee, H. (2018). Ultrathin IrO_2 nanoneedles for electrochemical water oxidation. Adv. Funct. Mater. *28*, 1704796. https://doi.org/10.1002/adfm.201704796.

40. Paul, D.K., and Karan, K. (2014). Conductivity and wettability changes of ultrathin nafion films subjected to thermal annealing and liquid water exposure. J. Phys. Chem. C *118*, 1828–1835. https://doi.org/10.1021/jp410510x.

Cell Reports Physical Science, Volume *4*

Supplemental information

Designing catalyst layer morphology for high-performance water electrolysis using synchrotron X-ray nanotomography

Jason Keonhag Lee, Pascal Kim, Kevin Krause, Pranay Shrestha, Manojkumar Balakrishnan, Kieran Fahy, Khalid Fatih, Nima Shaigan, Mingyuan Ge, Wah-Keat Lee, and Aimy Bazylak

Supporting Figures

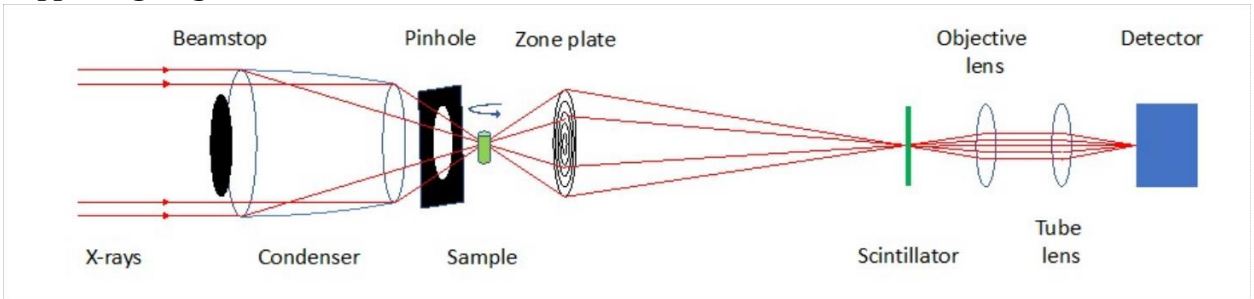

Figure S1. Schematic of the synchrotron X-ray nano computed tomography conducted in NSLS-II beamline.

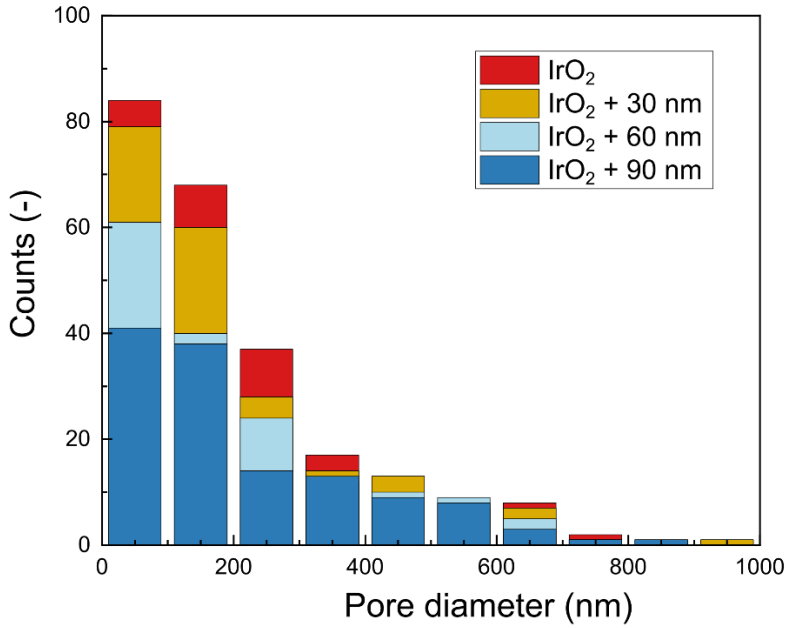

Figure S2. Pore size distributions of the iridium-based catalyst of (Sample 1) with varying ionomer layer thickness. Number of nano pores with the diameter less than 300 nm are significantly reduced with thicker ionomer layers, while the change in number of nano pores with diameters greater than 300 nm remains less sensitive to the ionomer thickness.

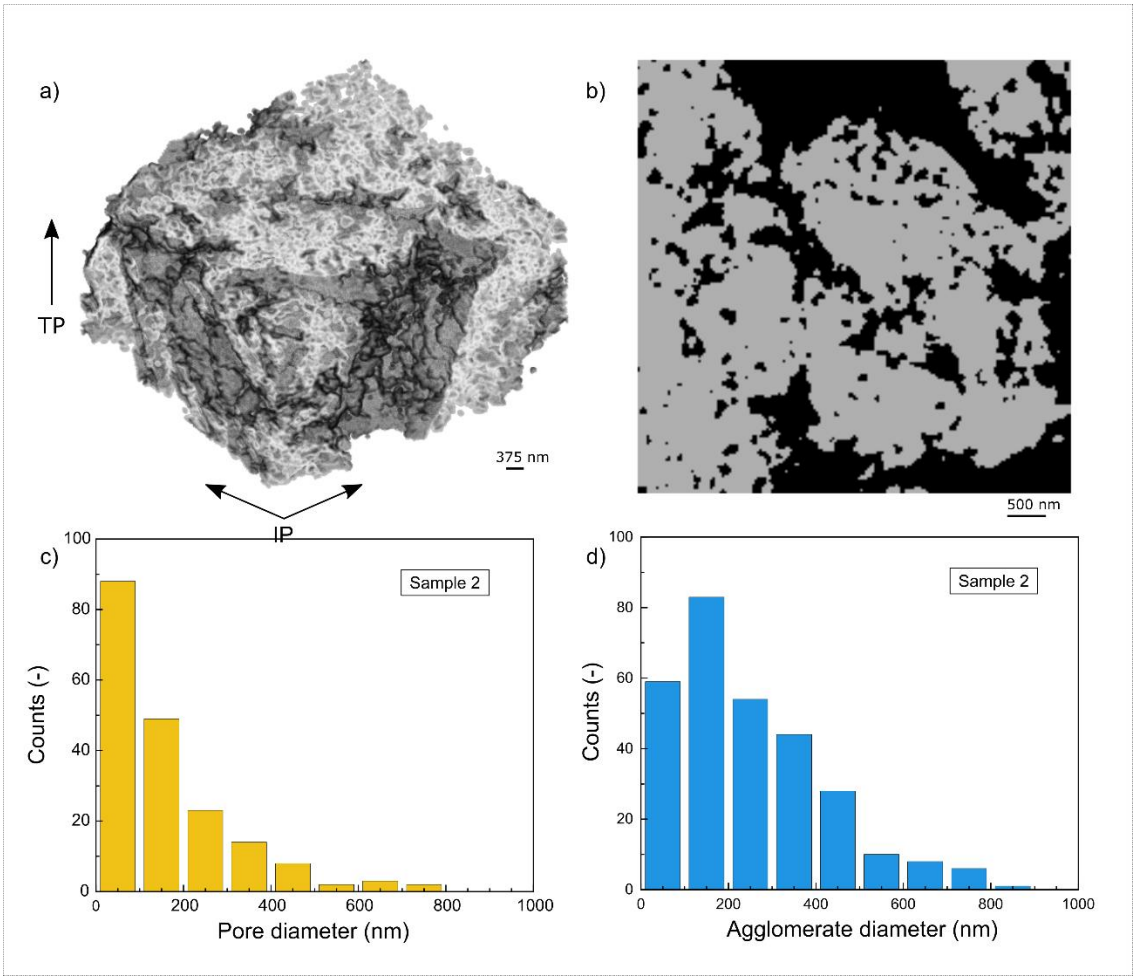

Figure S3. Structural characterization of the iridium-based catalyst (Sample 2). (a) 3D reconstruction of the iridium-based catalyst obtained via synchrotron TXM. Colors are used for visualization purposes only. (b) A cross-sectional image of Sample 2. (c) A pore size distribution and (d) an agglomerate size distribution of Sample 2.

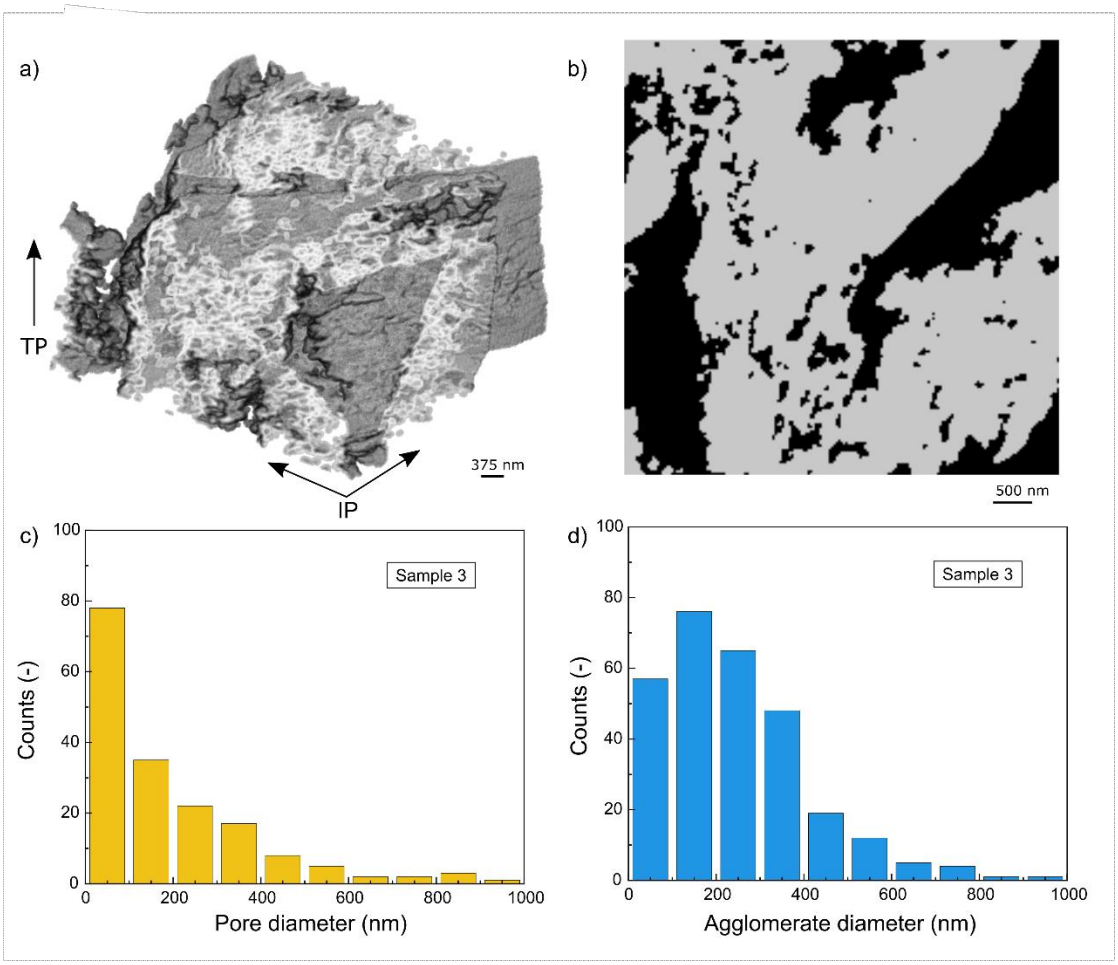

Figure S4. Structural characterization of the iridium-based catalyst (Sample 3). (a) 3D reconstruction of the iridium-based catalyst obtained via synchrotron TXM. Colors are used for visualization purposes only. (b) A cross-sectional image of Sample 3. (c) A pore size distribution and (d) an agglomerate size distribution of Sample 3. Similar trends in pore and agglomerate size distributions are seen for all the samples tested in this work (Sample 1, Sample 2, and Sample 3).

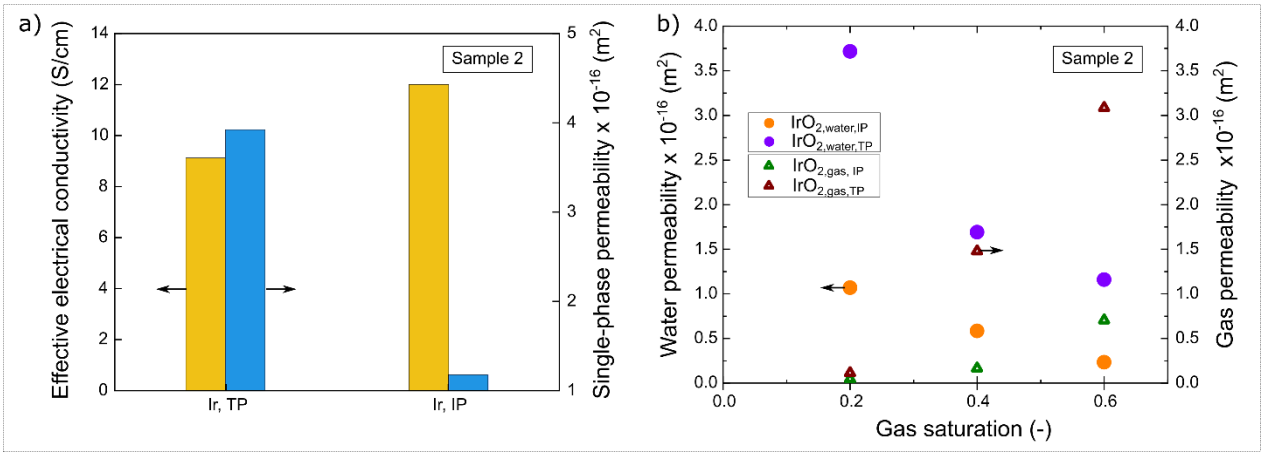

Figure S5. Comparing the electron conductivity and mass transport properties in in-plane and through-plane direction for Sample 2. (a) Effective electrical conductivity and single-phase permeability of Sample 2 in both in TP and IP direction. Transport in the catalyst structure takes place preferentially in the through-plane direction. (b) Two-phase permeability of liquid

water and gas as a function of gas saturation. The circle markers refer to the left y-axis (water permeability) and triangle markers refer to the right y-axis (gas permeability).

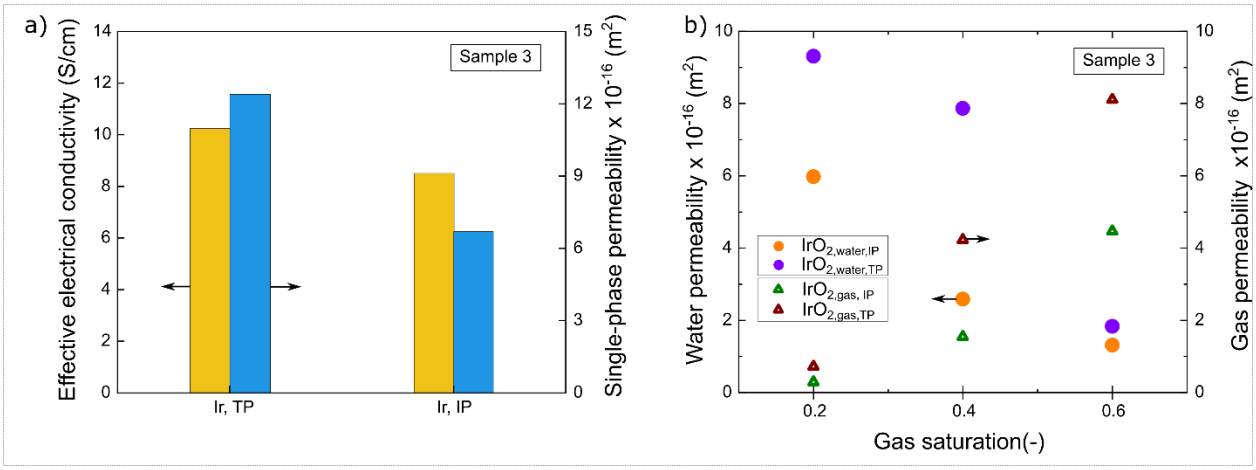

Figure S6. Comparing the electron conductivity and mass transport properties in in-plane and through-plane direction for Sample 3. (a) Effective electrical conductivity and single-phase permeability of Sample 3 in both in TP and IP direction. Transport in the catalyst structure takes place preferentially in the through-plane direction. (b) Two-phase permeability of liquid water and gas at varying gas saturation. The circle markers refer to the left y-axis (water permeability), and triangle markers refer to the right y-axis (gas permeability).

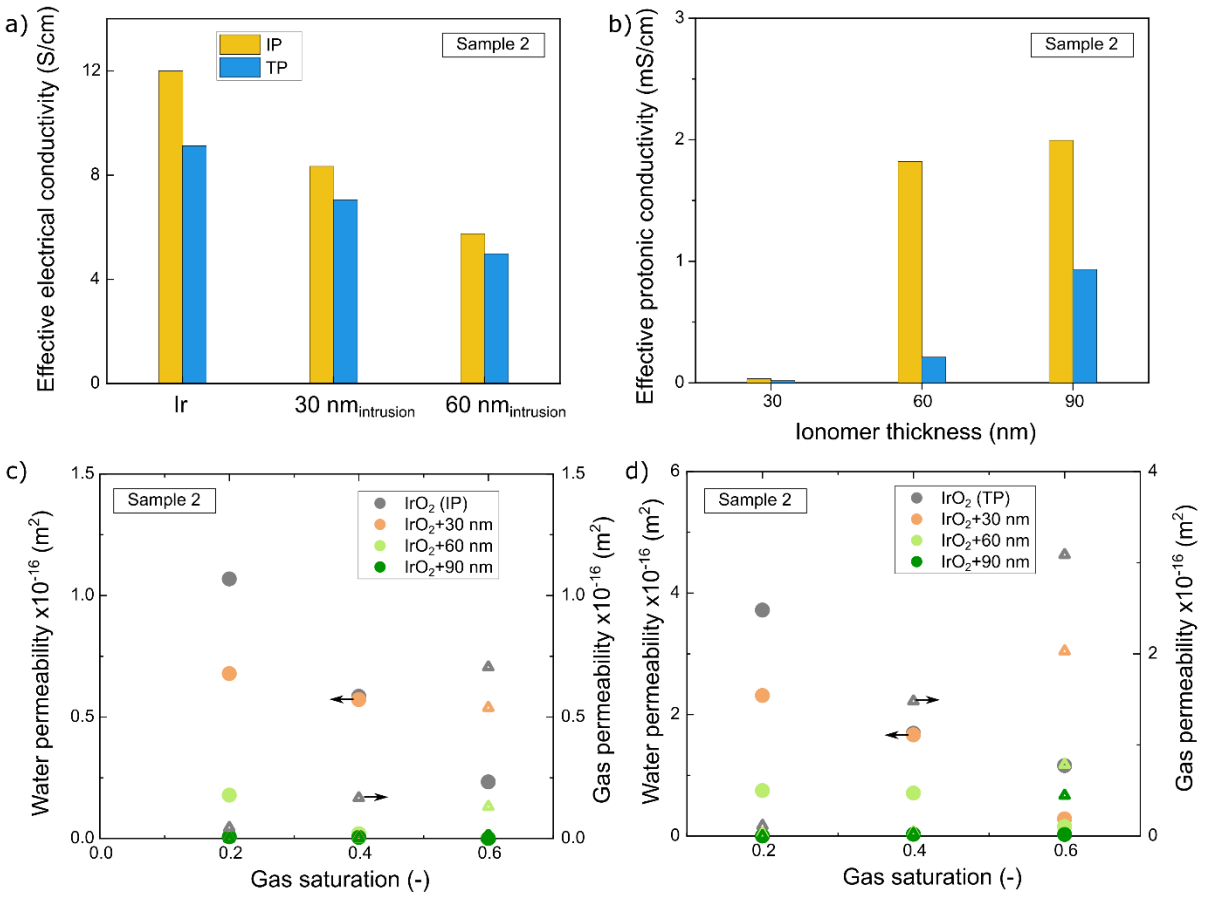

Figure S7. Characterization of Sample 2 with varying ionomer layer thicknesses. (a) Changes in effective electrical conductivity in the presence of an ionomer layer. (b) Effective protonic conductivity with varying ionomer layer thicknesses. (c) Two-phase permeability of gas and liquid water at varying levels of gas saturation in the in-plane direction and (d) in the through-plane direction. The circle markers refer to the left y-axis (water permeability), and triangle markers refer to the right y-axis (gas permeability).

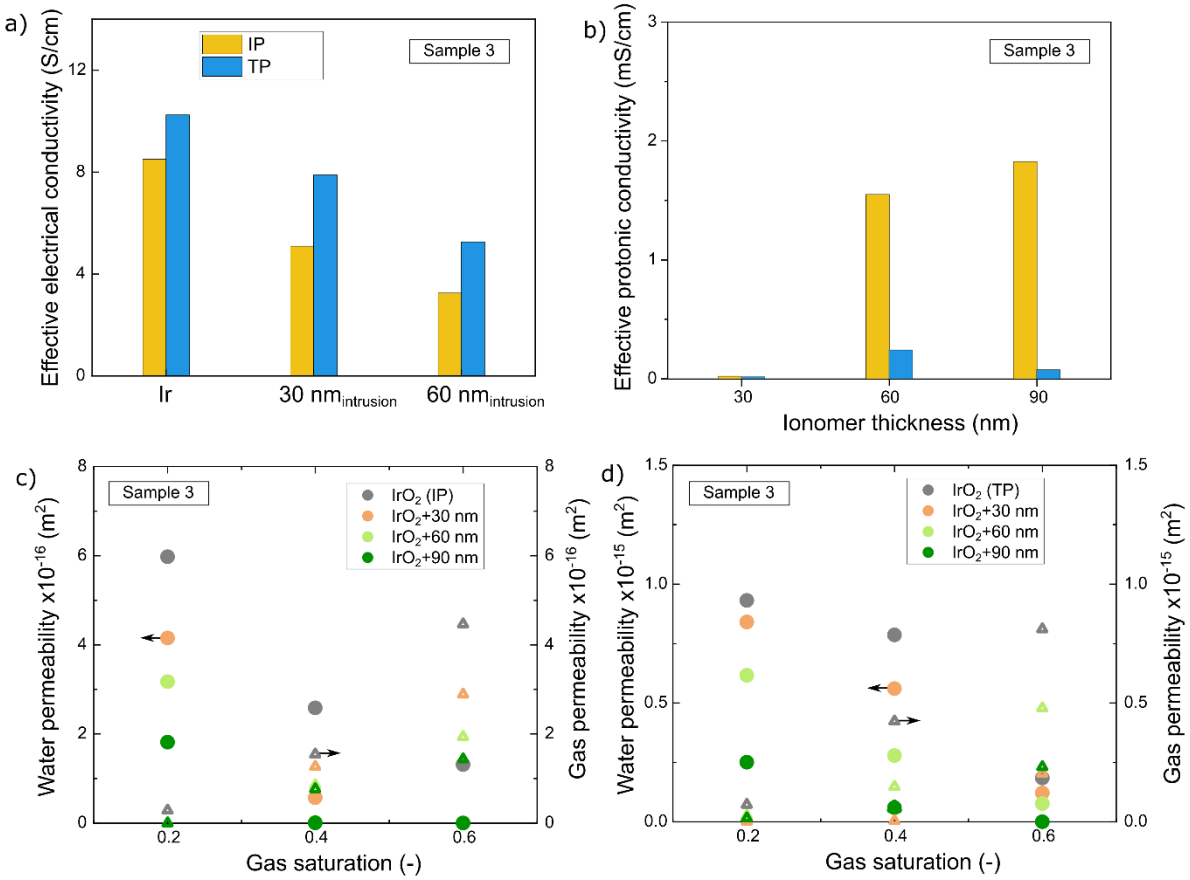

Figure S8. Characterization of Sample 3 with varying ionomer layer thicknesses. (a) Changes in effective electrical conductivity in the presence of an ionomer layer. (b) Effective protonic conductivity with varying ionomer layer thicknesses. (c) Two-phase permeability of gas and liquid water at varying levels of gas saturation in the in-plane direction and (d) in the through-plane direction. The circle markers refer to the left y-axis (water permeability), and triangle markers refer to the right y-axis (gas permeability).